Electronic Supporting Information

Influence of Perfluorinated Ionomer in PEDOT:PSS on the Rectification and Degradation of Organic Photovoltaic Cells

1. Experimental Section

1.1. Materials

Perfluorinated ionomer resin solution (PFI, Nafion® DE 520, 5 wt % in a mixture of aliphatic alcohols and aqueous solution, 45 % water, with a density of 0.924 g/mL at 25 °C) was purchased from Sigma-Aldrich with the following HPLC grade solvents: hydrochloric acid (HCl, 37 %), acetone, isopropanol and chlorobenzene. Poly(3,4-ethylenedioxythiophene):poly (styrenesulfonate) (PEDOT:PSS, 1:6 weight ratio, 1 g/L; AI4083) and regioregular poly(3-hexylthiophene) (P3HT, M_w = 57 kDa, *pdi* = 2.9) were obtained from Clevios and Rieken Metals, respectively. The soluble fullerene [6,6]-phenyl-C_{61} butyric acid methyl ester ($PC_{61}BM$) with > 99 % purity was supplied by Solenne BV Groningen. Indium tin oxide (ITO) coated glass substrates (15 Ω/square) were acquired from Xin Yan Technology Ltd. The UV optical adhesive (Norland Optical Adhesive 68) and coverslips for encapsulation were purchased from Thorlabs and Fisher Scientific, respectively.

1.2. OPV Devices

1.2.1. Device Fabrication

ITO-coated glass substrates were masked with a 4-mm-wide adhesive tape and etched in HCl acid (37 %) for 20 minutes. Having etched away the unwanted ITO, the patterned substrates were taken out of the HCl acid and rinsed in deionised water. The adhesive tape was removed from the substrates, leaving behind 4-mm-wide ITO strips. Any glue left on the substrates from the adhesive tape was cleaned with cotton buds and acetone. Further cleaning was completed by 15 minutes successive sonication in acetone, followed by isopropanol and finally deionised water. The substrates were then dried with nitrogen and placed in an oxygen plasma cleaner for 5 minutes.

PEDOT:PSS and PFI were used as received. Blend solutions were prepared by weight ratio using the weight concentrations provided by the manufacturer (1:6 and 5 wt % for PEDOT:PSS and PFI, respectively). The weight ratios are presented as PEDOT:PSS:*x*, with *x* either 1, 2.5, 6.0, 13.4 or 30. A PEDOT:PSS:PFI weight ratio of 1:6:1 was prepared by adding 10.8 μL of PFI solution to 3.5 mL of PEDOT:PSS. The volume of PFI solution to be added to 3.0 mL of PEDOT:PSS for *x* equal to 2.5, 6.0, 13.4 or 30 was 23.2, 55.7, 124.3 or 278.3 μL, respectively. The PEDOT:PSS:PFI solutions were left to stir vigorously overnight.

Sonicated and filtered (pore size 0.45 μm) PEDOT:PSS based solutions were spin-coated at 4000 rpm for 1 minute on quartz or ITO coated glass substrates. The substrates were placed on a hotplate at 120 °C for 15 minutes in a nitrogen-filled glovebox. A 20 mg/mL chlorobenzene solution of P3HT:PC_{61}BM at a weight ratio of 1:1 (5:5 mg dissolved in 0.5 mL) that was stirred gently overnight in the glovebox was spin-coated at 1000 rpm onto the PEDOT:PSS based thin films. The films were annealed, but allowed to cool prior to this step. This was followed by another annealing step at 130 °C for 15 min before placing the samples in the evaporator for the back electrode deposition. A 2-mm-wide 200-nm-thick aluminium electrode was thermally evaporated at 0.4 nm/s under a $2x10^{-6}$ mbar vacuum. The electrode overlap defines solar cells with an area of 0.08 cm^2. Organic photovoltaic (OPV) cells without PFI were also encapsulated using a UV-activated optical adhesive and glass cover slip. Encapsulated or not, the OPVs were removed from the glovebox, masked and characterised in air using a Keithley 2400 SMU and a K.H. Steuernagel AM1.5G solar simulator at 100 mW/cm^2. The illumination intensity was verified using a KG-5 NREL-calibrated monocrystalline silicon detector.

1.2.2. Device Characterisation and Degradation

The degradation study involved illuminating a solar cell continuously for a maximum of 24 h in air. A LabView program performed a J-V sweep between -1 and 1 V every 30 minutes. The performance parameters were extracted from the *J-V* curves and the power conversion efficiency (*PCE* or *η*) determined with the equation:

$$\eta = \frac{V_{OC} I_{SC} FF}{P_{in}} \tag{S1}$$

where V_{OC} is the open-circuit voltage, I_{SC} the short-circuit current, *FF* the fill factor, and P_{in} the incident illumination power. The external quantum efficiency (*EQE*) was measured using an incident photon-to-current efficiency (IPCE) setup, consisting of an NPL-calibrated photodiode, a Keithley 6517A picoammeter and a Bentham TMc300 monochromator.

1.3. Characterisation Techniques

1.3.1. Atomic Force Microscopy and Microscopic Kelvin Probe Measurements

Topography and work-function data were acquired with a Park Systems (XE-100) scanning probe microscope (SPM) using conductive Pt-coated Si cantilevers (NT-MDT). Measurements were performed inside a nitrogen-filled glovebox at ambient temperature. Prior to SPM characterisations, the samples were placed on a hot plate and annealed for 20 minutes at 120 °C to remove H_2O adsorbates. Topography and KPFM were recorded

simultaneously in AC mode with a resonant frequency of 280 kHz and by applying an AC modulation voltage of 2 V at 20 kHz, respectively. To estimate the sample work-function, the 4.7 eV Pt-coated Si cantilever was calibrated with a reference sample of highly ordered pyrolytic graphite (HOPG). The work-function ($W_{\text{f-KPFM}} = W_{\text{sample}}$) was determined by measuring the contact potential difference (V_{CPD}) and the calibrated work-function of the cantilever (W_{tip}), using the relation:

$$V_{\text{CPD}} = \frac{(W_{\text{tip}} - W_{\text{sample}})}{q} \qquad (S2)$$

where q is the electronic charge of an electron.[1-5]

1.3.2. Macroscopic Kelvin Probe Measurements

Work-function measurements were performed using a Kelvin probe (FAC-1, RIKEN KEIKI). The value recorded was for an area of 1 cm^2. Gold plates of 5.10 eV were used for the calibration.

1.3.3. Optical Transmission

Transmission measurements were recorded with a Perkin-Elmer Lambda 950 UV/Vis/NIR spectrometer with ITO coated glass substrates as references.

1.3.4. Wetability Characterisations

Contact angle measurements were performed using a contact angle goniometer (DM-501, Kyowa Interface Science Co. Ltd) and an environmental scanning electron microscope (ESEM) (Quanta FEG 250, FEI Co., OR, USA) equipped with a gaseous secondary electron detector (GSED) and Peltier cooling stage.

1.3.5. Film Thickness

Dektak stylus profilometer Veeco Model 150 was used to measure the organic film thicknesses.

2. Interfacial and Electronic Characterisations

2.1. Surface Morphology

Topography images were processed with a Fourier type filter to remove the weak signal frequency components of the electrical and mechanical noise. The 2D-power spectral densities (PSD) acquired by the Fourier transform, e.g. Figure S1 (a-b), were radially integrated to reflect the root mean squared (RMS) surface roughness. The resulting spectra, plotted both on logarithmic and linear scales, are presented in Figures S1c and S1d, respectively. Note that Figure 2b is a zoomed-in plot of Figure S1d. These figures show that the fluorination has a negligible influence on the surface roughness of the PEDOT:PSS based hole extraction layers (HELs), even though a subtle change is observed when [PFI]≈[PSS].

Consequently, the surface roughness cannot be responsible for

any variation in the device stability or efficiency.[4] The subtle change in topography observed in Figure 2b and S1d when [PFI]≈[PSS] is not evident in the RMS values shown in Table S1 and in Figure 2c. Although the HEL thicknesses acquired by Dektak stylus profilometer shown in Figure S2 appear to be larger when [PFI]>[PSS], the standard deviations overlap. Therefore, any alteration is minor. This has been confirmed by spectroscopic ellipsometry. Thus, like the surface roughness, HEL thickness cannot be responsible for the variations in the device stability and efficiency.
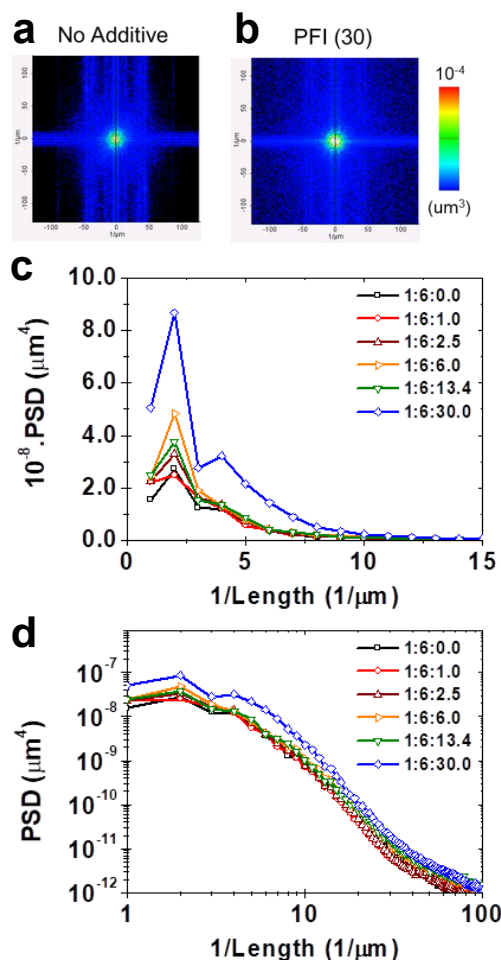
Figure S1.   (**a**) and (**b**) Radially integrated Fourier transforms for different concentrations of additive plotted on a linear scale. PSD profiles calculated from AFM measurements plotted on (**c**) linear and (**d**) logarithmic scales.

Table S1. Root mean squared (RMS) surface roughness values acquired by atomic force microscopy (AFM).

PEDOT:PSS:PFI loading (wt%)	RMS
1:6:0.0 (0.00)	1.5 ± 0.1
1:6:1.0 (12.50)	1.5 ± 0.1
1:6:2.5 (26.32)	1.6 ± 0.1
1:6:6.0 (46.15)	1.7 ± 0.3
1:6:13.4 (65.69)	1.7 ± 0.2
1:6:30.0 (81.08)	2.5 ± 0.1

Figure S2. Thickness of the HEL (PEDOT:PSS:PFI) measured by Dektak stylus profilometer for different concentrations of the additive.

2.2. Work-function

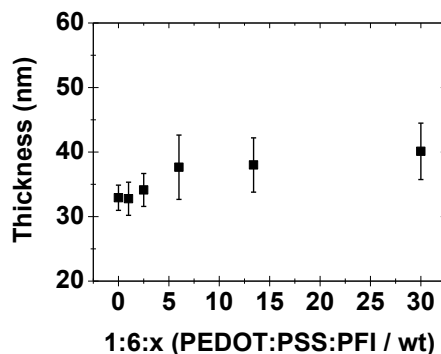The effect of PEDOT:PSS fluorination on the HEL thin film work-function in Table S2 presents the values obtained by both microscopic and macroscopic Kelvin probe measurements. The work-function remains unaffected by the fluorination until a threshold is reached. With both measurement techniques, the value of $x = 2.5$ is associated with a threshold beyond which the work-function of the HEL progressively increases.

Table S2. Microscopic and macroscopic work-function measurements acquired by KPFM and mKP, respectively.

PEDOT:PSS:PFI loading (wt%)	Wf (eV)-KPFM	Wf (eV)-mKP
1:6:0.0 (0.00)	4.71 ± 0.03	5.15 ± 0.02
1:6:1.0 (12.50)	4.78 ± 0.03	5.18 ± 0.02
1:6:2.5 (26.32)	4.73 ± 0.04	5.15 ± 0.02
1:6:6.0 (46.15)	5.25 ± 0.03	5.29 ± 0.02
1:6:13.4 (65.69)	5.23 ± 0.05	5.53 ± 0.02
1:6:30.0 (81.08)	5.41 ± 0.03	5.71 ± 0.01

2.3. Wetability Properties

The contact angle of deionised (DI) water on the HEL thin films was quantified for a range of PFI contents to study the influence of PEDOT:PSS fluorination. The Young and Dupré equations, Eq. S7 and S8 respectively,[6] were used to obtain Eq. S9 and quantify the adhesion energy of the DI water on top of PEDOT:PSS:PFI thin films.

$$\gamma_{SV} = \gamma_{SL} + \gamma_{LV}\,cos\,\theta_c \qquad (S3)$$

$$E_{adh} = \gamma_{SV} + \gamma_{LV} - \gamma_{SL} \qquad (S4)$$

$$E_{adh} = \gamma_{LV}\left(1 + cos\,\theta_c\right) \qquad (S5)$$

with the solid-vapor (γ_{SV}), solid-liquid (γ_{SL}) and liquid-vapor (γ_{LV}) interfacial tensions. θ_c is the equilibrium contact angle of the drop on top of the surface. The adhesion energy, E_{adh}, is the amount of energy needed to separate the liquid from the surface. From a practical point of view, γ_{LV} is the DI water surface tension, which is 71.99 mN/m at 25 °C.[7] Six contact angle measurements were performed using the Sessile Drop method (0.3 µl, tangent) for each fluorination concentration. The mean contact angles are listed in Table S3. A nearly constant value up to $x = 2.5$ wt % is observed followed by a progressive and moderate decrease of the surface energy for PEDOT:PSS layer fluorinations varying between $x = 6$ and 30 wt %.

Table S3. Contact angle (θ_c) variation with PEDOT:PSS fluorination and adhesion energy, E_{adh}, calculated with Eq. S9.

PEDOT:PSS:PFI loading (wt%)	θ_c (°)	E_{adh} (mN/m)
1:6:0.0 (0.00)	11.1 ± 0.4	142.6 ± 0.1
1:6:1.0 (12.50)	11.1 ± 0.5	142.6 ± 0.1
1:6:2.5 (26.32)	11.8 ± 1.1	142.5 ± 0.3
1:6:6.0 (46.15)	26.7 ± 1.2	136.3 ± 0.7
1:6:13.4 (65.69)	33.5 ± 3.3	132.0 ± 2.3
1:6:30.0 (81.08)	35.9 ± 2.9	130.3 ± 2.2

3. Device Characterisation

3.1. Analysis Principles

To characterise a photovoltaic cell, a current-voltage measurement is performed in the dark and under illumination, as described in Section S1.2. The dark current for an ideal photovoltaic cell is equivalent to a standard diode:[8]

$$I = I_s\left(exp\left(\frac{qV}{nk_BT}\right) - 1\right) \qquad (S6)$$

where I is the diode current, I_s the dark saturation current, q the elementary charge, V the applied voltage, n the ideality factor, T the temperature and k_B the Boltzmann constant.

Though developed for inorganic photovoltaics, the equivalent circuit model based on elementary circuit elements can help understand, and in certain circumstances predict, the current-voltage characteristics of OPVs under illumination.[9-11] The equivalent circuit for an ideal and practical cell under illumination are shown in Figure S3a and S3b, respectively.

Principally, the model can assist in elucidating the loss mechanisms that influence the FF,[12] a very important performance parameter which is defined as the ratio between the maximum power output and the theoretical maximum obtainable power that the photovoltaic cell can deliver. It is a quintessential measure of performance of a photovoltaic cell, as it describes the efficiency at which the carriers are extracted out of the device.
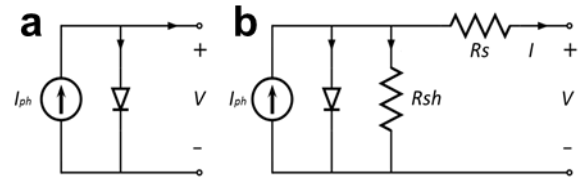

Figure S3. Equivalent circuit for an ideal **(a)** and practical **(b)** photovoltaic cell under illumination.

The shape of the current-voltage characteristic for an ideal photovoltaic cell, Figure S3a, under illumination remains solely dependent on the diode, as shown in Equation S15.

$$I = I_s\left(exp\left(\frac{qV}{nk_BT}\right) - 1\right) - I_{ph} \qquad (S7)$$

where I_{ph} is the photo-induced current subtracted from Equation S14. Thus, the loss mechanisms are related to T, n and I_s. T can be ignored as the temperature is altered neither from device to device, nor during the current-voltage measurement, as shown later in Section S.3.3.3. The ideality factor, n, is related to the dissociation and recombination of excitons,[13] whilst the saturation current, I_s, is proportional to the difference between the highest occupied molecular orbital (HOMO) level of the donor and the lowest unoccupied molecular orbital (LUMO) level of the acceptor.[14-16] In the present study, these molecular orbitals, too, have no influence on the variation of the device performance, as the use of PFI in the HEL changes neither the composition nor the morphology of the active layer.[4]

A practical equivalent circuit representation of photovoltaic cells, as shown in Figure S3b, involves series and parallel parasitic resistances in addition to the current source and diode. These resistances, R_S and R_{Sh}, denote the voltage and current losses in the device, respectively. Hence, the corresponding cell response is given by:[8, 17]

$$I\left(1 + \frac{R_s}{R_{sh}}\right) - \frac{V}{R_{sh}} = I_s\left(exp\frac{q}{nk_BT}(V - IR_s) - 1\right) - I_{ph} \qquad (S8)$$

Typically, the contact resistances between the active layer, interlayers, charge transport or extraction layers and electrodes, and the bulk resistances of the aforementioned are responsible for R_S; whilst the parameters that influence current leakage and the recombination of charge carriers, such as the active layer thickness, illumination intensity, and interfacial morphology, are

responsible for R_{Sh}.[12][18] Both R_S and R_{Sh} impact the squareness of the *J-V* characteristic curves, limit the *FF* and, by extension, the *PCE* of OPVs. The latter resistance less so, as it reduces the V_{OC} and accounts for current losses in the cell, whereas R_S reduces the J_{SC} and indicates if the current largely flows through the diode or is diverted to the external load.

To maximise the device performance, one would like to reduce R_S, i.e. the loss of voltage due to the external load resistance. It results in an increase of the voltage across the diode, thus quickens the response of *J* with *V*, making the *J-V* characteristic more square-shaped. By reducing the current leakage the R_{Sh} value increases. In the best-case scenario, i.e., R_S and R_{Sh} equal 0 and ∞, respectively, one recovers equation S15 from S16. Various methods are used in the literature to extract the device resistances, and one of the most popular methods is to take the reciprocal of the slope around $V=0$ and V_{max}, for R_{Sh} and R_S, respectively;[12] This approach is used in the present work.

3.2. Additional Concentrations

The use of PFI as an additive in PEDOT:PSS can accelerate the charge extraction in P3HT:PC$_{61}$BM OPVs.[4] This was evidenced by transient absorption and work-function measurements. We note that the accuracy of R_S and R_{Sh} prevents one from using them for shedding light on the mechanisms responsible for this improvement; this is a topic beyond the scope of this manuscript. Nonetheless, in the present study, the resistance analysis does provide insights into the lower J_{SC} and *FF* values acquired at low PFI concentrations. The lowest J_{SC} and *FF* value occurs at a PEDOT:PSS:PFI weight ratio of 1:6:2.5, leading to a PCE of 1.04 %. This indicates a considerable reduction, when compared to the PCE obtained without PFI that is 2.53 %, which is a result of the J_{SC} decreasing from 8.84 to 6.12 mA/cm^2 and the *FF* from 48.6 to 28.08 %. Whilst a significant leakage current is observed, i.e., dark-current in Figure S4Figure S4 and small R_{Sh} in Table S4, it is the R_S and not the R_{Sh} that is largely responsible for the deterioration of the device performance. The reason is that, as mentioned above, R_S reduces the J_{SC} and not the V_{OC}, whereas R_{Sh} reduces the V_{OC} and not the J_{SC}.
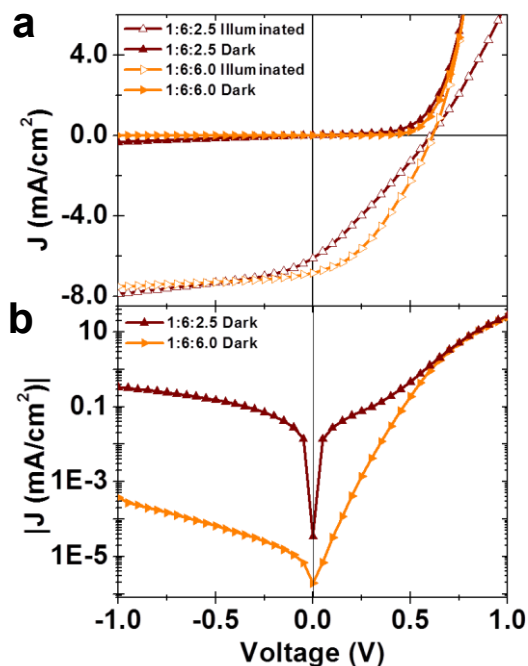

Figure S4. Current-voltage characteristics for P3HT:PC$_{61}$BM with a PEDOT:PSS:PFI weight ratio of 1:6:2.5 and 1:6:6.0 in the dark and under AM1.5G illumination at 100 mW/cm^2 **(a)**. Dark-current plotted on a semi-logarithmic scale **(b)**.

Table S4. Device performance parameters for P3HT:PC$_{61}$BM devices with the selected PEDOT:PSS:PFI weight ratios: PFI content (x), series resistance (R_S), shunt resistance (R_{Sh}), short circuit current density (J_{SC}), open circuit voltage (V_{OC}), fill factor (*FF*), and power conversion efficiency (*PCE*).

x (wt%)	R_s ($\Omega.cm^2$)	R_{sh} ($k\Omega.cm^2$)	J_{sc} (mA/cm^2)	V_{oc} (mV)	*FF* (%)	*PCE* (%)
0.0	5.4	0.67	8.84	589	48.60	2.53
2.5	52.3	0.33	6.12	605	28.08	1.04
6.0	9.9	0.82	6.85	615	37.55	1.58
30.0	7.7	0.70	8.85	618	54.00	2.96

A low PFI content is then correlated with a large reduction in J_{SC} and a subtle change in the V_{OC}. As the series resistance decreases, the J_{SC} increases with larger concentrations of PFI. At a PEDOT:PSS:PFI weight ratio of 1:6:30, the J_{SC} has fully recovered. At first sight, this trend could be rather surprising as PFI is an insulator. Thus, one would expect an increase in R_S and a decrease in J_{sc} with increasing the PFI concentration if continuous variations were to be happening. Nonetheless, the most probable reason for this behaviour is that at low concentrations the PFI, a water soluble polymer, disperses around the PEDOT grains driven by the sulfonic acid groups and the entropy of mixing. Here, it mostly disrupts the PSS shell as well as the charge transport between the PEDOT grains, leading to a detrimental impact on the device performance. As the concentration increases above a PEDOT:PSS:PFI weight ratio of 1:6:2.5, aggregates of PFI, driven by the amphiphobic nature of the fluorinated polymer, form and diffuse to the surface of the HEL. There, its electronegativity compensates for the above-mentioned impact by improving the charge extraction and, consequently, the device performance. This is supported by our OPV, contact angle and work-function measurements.

Disrupting the charge transport between the PEDOT grains is consistent with an increase in the resistivity of the PEDOT:PSS based HEL, R_S. An increase in R_S, whether brought about by an imbalance in the charge carrier mobilities, interfacial dipoles or defects, and energy barriers, can lead to an S-kink in the *J-V* characteristic.[19-24] In the present work, this S-kink is observed at a low PFI content and results in carrier accumulation within the device. It is largely responsible for the low *FF* asshown in Figure S4a and Table S5. As the PEDOT:PSS:PFI weight ratio is increased from 1:6:2.5 to 1:6:6, the *FF* recovers, and R_S goes from 52.31 to 9.88 $\Omega.cm^2$. The effect on the shape of the *J-V* characteristic is then significant, especially when considering the positive current in the forward bias direction. The J_{SC} increases from 6.12 to 6.85 mA/cm^2 and the V_{OC} from 0.605 to 0.615 V. The increase in V_{OC} comes about by reducing the current leakage, i.e., by decreasing the dark-current and increasing R_{Sh}, as shown in Figure S4b and Table S5, respectively. The *PCE* increases from 1.04 to 1.58 % and is the result of PFI content at the HEL and P3HT:PC$_{61}$BM interface. A similar abrupt change is observed in the contact angle and work-function. The contact angles for 1:6:0, 1:6:1 and 1:6:2.5 are 11.1, 11.1 and 11.8°, respectively, as presented in Table S2. At low PFI content, the variation of θ_c is small, but at 1:6:6 the contact angle abruptly changes to 26.7°. Similarly, the work-functions acquired by KPFM and mKP are relatively constant for the first three PFI additive concentrations, leading to 4.71, 4.78 and 4.73 eV, and 5.15, 5.18 and 5.15 eV, respectively. As observed with θ_c, at a PEDOT:PSS:PFI weight ratio of 1:6:6 the work-function values determined by KPFM and mKP reach 5.25 and 5.29 eV, respectively, and keep increasing for higher PFI content. The topography images recorded by AFM, Figure 2a, showed subtle changes with fluorination. Furthermore, the images were Fourier filtered and transformed to 2D Power Spectrum Density (PSD)

as presented in Figure S1ab. These were radially integrated to represent the root mean square (RMS) roughness of the sample and plotted on a logarithmic and linear scale, Figure 2b and S1c, respectively.

3.3. Degradation

Degradation measurements were performed on OPVs, as described in Section S1.2. Our investigation focused on the PEDOT:PSS:PFI weight ratios of 1:6:0, 1:6:1, 1:6:13.4 and 1:6:30, i.e., at low and high PFI contents. For a reliable analysis, we avoided the transition region between 1:6:2.5 and 1:6:6, which is revealed by contact angle and Kelvin probe measurements. The performance parameters FF, V_{OC}, J_{SC} and PCE extracted from the J-V sweeps are shown in Figure S5, S6, S7 and S8, respectively.

3.3.1. Time Evolution of the Raw FF, J_{SC}, V_{OC} and PCE

At 0 h, the FFs for 1:6:0, 1:6:1, 1:6:13.4 and 1:6:30 are 48.55, 30.76, 47.19 and 54.01 %, respectively. The cause of the 1:6:1 low FF has been discussed in Section S3.2. At high concentrations of PFI, improved charge extraction enhances the OPV performance and the FF is ~ 10 % higher than that without PFI.[4] The balance between the charge extraction and disrupted charge transport justifies that at lower PFI concentration, the FF is reduced, and for instance the value recorded for 1:6:13.4 is slightly lower than that for 1:6:0. As shown in Figure S5 and detailed in Table S5, after half an hour, the FF values decrease very slightly to 48.13, 46.16 and 52.73 % for 1:6:0, 1:6:13.4 and 1:6:30, respectively. The reduction in FF is moderately larger for the latter two concentrations, i.e., > 2.0 % compared with < 1.0 %. However, for 1:6:1,the FF increased to 31.15 %. After an hour of operation, the FFs for 1:6:0, 1:6:1, 1:6:13.4 and 1:6:30 are 46.77, 31.92, 45.87 and 53.01 %, respectively. A slight decrease in FF is observed for 1:6:0 and 1:6:13.4 of almost 3 % and 1 %, respectively. The other two concentrations, 1:6:1 and 1:6:30, show a slight increase in FF.

Table S5. Fill factor (FF in %) as a function of time (t) for selected PEDOT:PSS:PFI weight ratios, x being the PFI content.

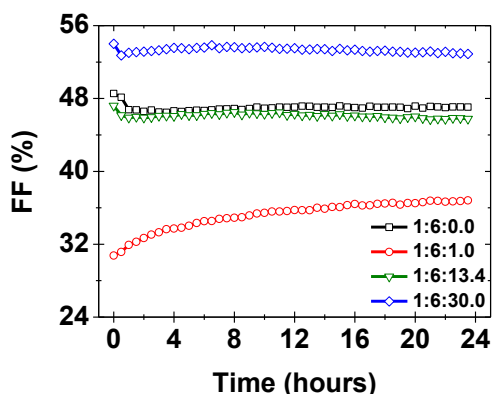| x wt%	t_0	$t_{0.5}$	t_{final}	% variation $t_{0-0.5}$	% variation $t_{0-final}$
0	48.6	48.1	47.1	-1.03	-3.09
1.0	30.8	31.1	36.8	+1.30	+19.48
13.4	47.2	46.2	45.8	-2.12	-3.03
30.0	54.0	52.7	52.9	-2.41	-2.04

Figure S5. Degradation study: Fill factor (FF) for OPV devices with different concentrations of PFI in the PEDOT:PSS based HEL. Data recorded at 30 min time intervals under continuous AM1.5G illumination at 100 mW/cm^2.

The FFs, with the exception of concentration 1:6:1, show a small decrease at very short running time. Not observing such a decrease for 1:6:1 might result from the initial decay having already occurred before the J-V sweep. After an hour of operation, the change in FF is negligible for 1:6:0, 1:6:13.4 and 1:6:30 with the last FFs recorded as 47.06, 45.76 and 52.89, respectively. The percentage decrease between the initial and final measurement is around 3 % for all additive concentrations, with the exception of 1:6:1, which shows a strong percentage increase from less than 20 % to 36.8 %. A possible explanation for this large increase is a decrease in the charge extraction efficiency at the cathode. This may arise from oxidation or delamination of the back electrode.[25-29] A back electrode alteration would result in a more balanced charge extraction and thus an increase in the FF. This would also be consistent with the hole accumulation reported in some P3HT:PC$_{61}$BM devices.[30-32] However, if this were simply to be the case, a decrease in FF would be observed for the devices that possess balanced charge extraction right after their fabrication. An alternative explanation is that there is a progressive increase of the hybrid HEL layer conductivity and the progressive formation of a dipole layer at the HEL-P3HT:PC$_{61}$BM interface due to the PFI molecules. It could occur through the water molecule brought in by the hygroscopic sulfonic acid groups of the PFI additive that counteracts the disruption of charge transport at low concentrations of PFI between the PEDOT grains.[33-36] The resulting progressive increase in the charge extraction efficiency at the anode is attributed to the FF recovery mechanism described in Section S3.3.4. More importantly, the mechanisms responsible for P3HT:PC$_{61}$BM degradation have a minor influence on the FF, as shown in Table S6 and in Figure S5. The use of PFI as additive to PEDOT:PSS improves the stability of OLEDs and OPVs, and one explanation which has been presented so far is that this stability gain could be achieved by preventing the acidic PSS from etching the ITO and blocking the diffusion of metal ions (In and Sn) into the HEL.[4, 37-39] This is nonetheless questionable as PFI molecules also present the same sulfonic acid groups as PSS, and furthermore if this were the case, there would be a significant decrease in the FF when the anode metal ions were diffusing, as demonstrated with nanoparticles or isolated metal islands.[40-44]

Focusing now on the open-circuit voltage presented in Figure S6, we note that for most devices, after a first V_{OC} decay, its value stabilises. Due to the S-kink described in Section 3.2, the 1:6:1.0 concentration appears as an exception with a partial recovery after the initial V_{OC} drop. To simplify the analysis, only the first, the half an hour and final measurements are more specifically discussed and presented in Table S6. For the 1:6:0.0 device, the initial decay is very fast, almost exponential lasting only for the first half an hour, until the V_{OC} reaches a stable value. The overall V_{OC} decay corresponds to a decrease of the order of 3 %. The percentages of decrease for 1:6:1 and 1:6:13.4 are larger than that of 1:6:0, while a smaller percentage decrease is obtained for 1:6:30.

Table S6. Open-circuit voltage (V_{OC} in V) as a function of time (t) for selected PEDOT:PSS:PFI weight ratios, where x is the PFI content.

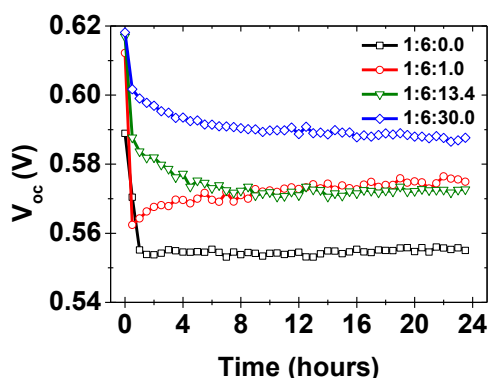| x (wt%)	t_0	$t_{0.5}$	t_{final}	% variation $t_{0-0.5}$	% variation $t_{0-final}$
0	0.589	0.570	0.555	-3.23	-5.77
1.0	0.612	0.562	0.574	-8.17	-6.21
13.4	0.617	0.588	0.572	-4.70	-7.29
30.0	0.618	0.602	0.587	-2.59	-5.02

Figure S6. Degradation study: Open-circuit voltage (V_{OC}) for OPV devices with different concentrations of PFI in the PEDOT:PSS based HEL. Data recorded at 30 min time intervals under continuous AM1.5G illumination at 100 mW/cm^2.

The V_{OC} percentage decrease from the end of the first half an hour to the last measurement are between 2 and 3 % for all PFI concentrations, and the total decrease between 5 and 8 %. If metal ion diffusion were to substantially reduce the V_{OC} in the 1:6:0 device, then a high concentration of these ions would have to enter the HEL within the first hour of operation. However, in this case much shorter time scales would be observed.[44] Furthermore, if PFI were to help preventing such a metal ion diffusion, it would only account for approximately half of the decrease observed in V_{OC}. The V_{OC} increase with fluorination content at t = 0 h is accomplished by improving the charge extraction at the anode.[4] The V_{OC} is then not the main performance parameter that influences the degradation, nor is it likely that the diffusion of metal ions is largely responsible for the reduction in V_{OC}.

As shown in Table S7 and in Section S3.2, and displayed in Figure S7, low concentrations of PFI result in a lower J_{SC} at t = 0 h. This strengthens the argument that PFI can, at low concentrations, disrupt the charge transport between the PEDOT grains, while the variation of the surface potential is not strong enough to extract the charges faster than in pristine HEL films. Similar behavior is observed when silver nanoparticles are incorporated into the PEDOT:PSS HEL.[44] The most noticeable result is that the use of PFI additives inhibits the fast exponential decay observed in the first half an hour of operation with the 1:6:0 device. Table S7 shows that the J_{SC} percentage decreases by about one order of magnitude between 1:6:0 and 1:6:30. However, as illustrated in Figure S7, PFI does not significantly alter the J_{SC} slow decay with operation time. The J_{SC} slopes taken between 8 h of operation and the final characterisation time for 1:6:0, 1:6:1, 1:6:13.4 and 1:6:30 are -0.036, -0.046, -0.046 and -0.054, respectively, with an uncertainty of ±0.001. Consequently, for the longer operation time, the OPVs containing PFI decay slightly faster than that without PFI.
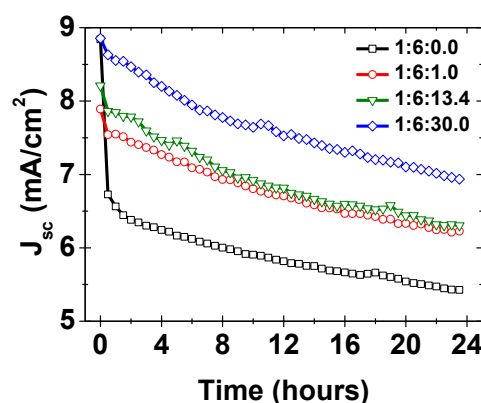

Figure S7. Degradation study: Short-circuit current density (J_{SC}) for OPV devices with different concentrations of PFI in the PEDOT:PSS based HEL. Data recorded at 30 min time intervals under continuous AM1.5G illumination at 100 mW/cm^2.

Overall, including J_{SC}, FF and V_{OC}, the results indicate that the PFI slows down the degradation mechanism responsible for the fast decay, but does not prevent degradation completely nor indefinitely. The encapsulated device results shown in Figure S15 support this argument and advocate that the fast decay is related to the hygroscopic nature of the HEL. The use of PFI may, in addition to inhibiting H_2O from altering the properties of the HEL, i.e., work-function and conductivity etc.,[33, 36] prevent H_2O from diffusing from the HEL through the active layer to the back electrode.[45] As a lipophobic polymer, PFI does not mix with the active layer, while the hydrophobic property of its fluorinated chains inhibits the diffusion of H_2O.

The *PCE* variation presented in Table S8 and Figure S8 illustrates that except for $x = 1.0$, all the devices deteriorate over time. As seen in the J_{SC} curves, the main difference in the *PCE* variation over time is in the early stage of the degradation. Indeed, PFI considerably reduces the initial fast exponential decay by inhibiting the degradation of the J_{SC}. Nonetheless, the decrease in J_{SC} occurs in conjunction with that in the FF and V_{OC}, and a combination of these effects leads to the sudden drop in *PCE* observed after half an hour of operation in Figure S8. As in the case of J_{SC}, PFI concentrations do not induce significant change in the slow decay of *PCE* that occurs over longer time scale. The case of $x = 1.0$ stands out among the others, but only because of the initial S-kink, which resorbs over the device usage time leading to effect cancellations between J_{SC}, FF and V_{OC}. It should nonetheless be noted that the highest PFI concentration investigated in this study both increases the device efficiency by about 15 % at t = 0 h, and slows down its degradation so much that its *PCE* is > 30 % more than the value of the pristine PEDOT:PSS based device after ~ 24 h of operation.

Table S7. Short-circuit current density (J_{SC} in mA/cm^2) as a function of time (t) for the selected PEDOT:PSS:PFI weight ratios, where *x* is the PFI content.

x (wt%)	t_0	$t_{0.5}$	t_{final}	% variation $t_{0-0.5}$	% variation $t_{0-final}$
0	8.84	6.72	5.43	-23.98	-38.58
1.0	7.89	7.54	6.23	-4.44	-21.04
13.4	8.21	7.86	6.30	-4.26	-23.26
30.0	8.85	8.63	6.93	-2.49	-21.69

Table S8. Power-conversion efficiency (*PCE* in %) as a function of time (t) for the selected PEDOT:PSS:PFI weight ratios, where *x* is the PFI content.

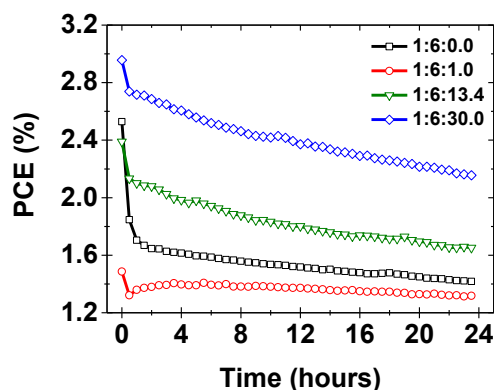| x (wt%)	t_0	$t_{0-0.5}$	t_{final}	% variation $t_{0-0.5}$	% variation $t_{0-final}$
0	2.53	1.85	1.42	-26.88	-43.87
1.0	1.49	1.32	1.32	-11.41	-11.41
13.4	2.39	2.13	1.65	-10.88	-30.96
30.0	2.96	2.74	2.15	-7.43	-27.36

Figure S8. Degradation study: Power conversion efficiency (*PCE*) for OPV devices with different concentrations of PFI in the PEDOT:PSS based HEL. Data recorded at 30 min time intervals under continuous AM1.5G illumination at 100 mW/cm^2.

Overall, the decreases in *FF* and V_{OC} are not significant considering that the decrease in *PCE* for 1:6:0.0 is ~ 26.88 % within the first half an hour. The majority of which arises from the decrease in J_{SC} of ~23.98 %. That said, having significantly reduced that which is responsible for the degradation, i.e. J_{SC} shown in Figure S7, the decrease in FF and V_{OC} do play an important role in the first half an hour, as the percentage decrease in *PCE* is 7.43 % for 1:6:30, i.e. accounts for 2/3 of the degradation in *PCE*. The initial and fast degradation of OPV devices is referred to as "burn-in" time. It is often characterised by an almost exponential *PCE* decay, which is followed by a slower and more linear deterioration. Whilst identifying the physical mechanisms involved in the burn-in is made difficult by the fact that the burn-in magnitude and duration vary from one OPV systems to another,[46-50] the measurements herein reported show that for the ITO/PEDOT:PSS/P3HT:PC$_{61}$BM/Al architecture, it is the PEDOT:PSS HEL that is largely responsible for the burn-in.

3.3.2. Shunt and Series Resistances

Table S9. R-series/shunt for the P3HT:PCBM devices at 0, 0.5 and after 24 h. Loading of PEDOT:PSS in % wt.

PFI (wt %)	R series ($\Omega.cm^2$)	R shunt ($k\Omega.cm^2$)
0.0	5.4 / 6.9 / 8.4	0.67 / 0.91 / 0.90
1.0	6.1 / 6.5 / 11.4	0.54 / 0.45 / 0.57
13.4	5.0 / 4.9 / 9.4	0.74 / 0.77 / 0.70
30.0	7.7 / 8.0 / 10.8	0.70 / 1.06 / 0.76

Table S10. Percentage increase/decrease in R-series/shunt for the P3HT:PCBM devices 0 to 0.5 h, 0.5 to 24 h and 0 to 24 h. Loading of PEDOT:PSS in % wt..

PFI (wt %)	R series (%)	R shunt (%)
0.0	27.0 / 21.5 / 54.3	35.0 / 0.66 / 34.1
1.0	6.4 / 74.5 / 85.6	15.6 / 25.6 / 6.0
13.4	2.2 / 92.7 / 88.4	3.5 / 8.5 / 5.3
30.0	3.3 / 36.2 / 40.6	50.9 / 28.6 / 7.7

3.3.3. Selected *J-V* Characteristics

The hygroscopicity, acidity and chemical reactivity of PEDOT:PSS has prompted research into its replacement.[45, 51] To address these issues, researchers have tried various inorganic alternatives, which include but are not limited to: MoO_3, WO_3 and V_2O_5.[52-55] Whilst progress has been made in using these materials, they typically require high temperature vacuum processing. This is not compatible with the solution-processable, large-area, high throughput and cost-effective concept of OPVs. Organic replacements have also been considered; however, successful contenders are scarce.[56] The low cost, tuneability and availability of PEDOT:PSS makes it an ideal candidate for an electrode or HEL in OPVs. The use of additives, for example PFI, show potential to be effective in tuning the properties of PEDOT:PSS for improved efficiency and stability. The *J-V* characteristics used in the aforementioned analysis are shown in Figure S9. Figure S9a illustrates a considerable reduction in J_{SC} when no additive is used in the PEDOT:PSS HEL after half an hour of operation. This degradation in J_{SC} is the result of the hygroscopic PEDOT:PSS, the exclusion of which has been shown to remove the initial fast decay.[45] The other Figures, Figures S9b, S9c and S9d obtained for 1:6:1, 1:6:13.4 and 1:6:30, respectively, show a minor decrease in the J_{SC}.
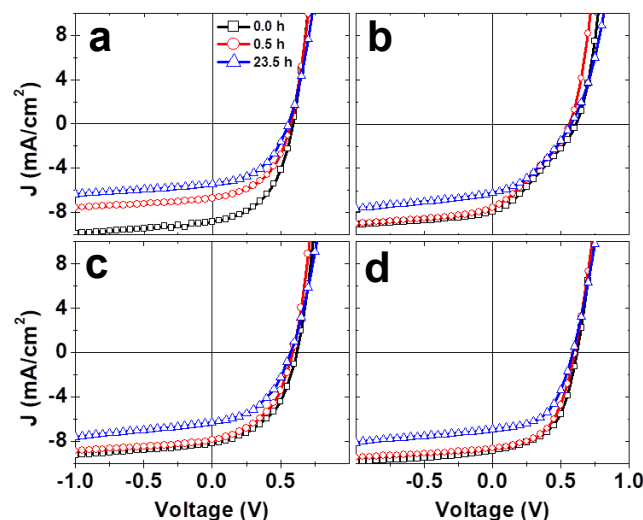

Figure S9. Degradation study: Current-voltage characteristics for P3HT:PC$_{61}$BM without the additive (**a**) or with additives at a PEDOT:PSS:PFI weight ratio of 1:6:1.0 (**b**), 1:6:13.4 (**c**) and 1:6:30.0 (**d**) at 0.0, 0.5 and 23.5 h of continuous AM1.5G illumination at 100 mW/cm^2.

Photochemical reactions in the active layer have been shown to degrade the *FF*, J_{SC} and V_{OC}. However, their influence on J_{SC} was shown to be subtle for the first half an hour of operation.[45, 47] Thermochemical and morphological changes can also arise in the active layer, but their effects on J_{SC} are minor as the measurements are performed at room temperature and the temperature is not altered during the measurements, as shown in Section S3.3.3.[57-60] The characterisation of the encapsulated device shown in Section S3.3.5 also supports this argument. Other mechanisms responsible for the decrease in V_{OC} and *FF* reported in the literature concern mostly the aluminium back electrode. Degradation at this electrode can occur by means of oxidation, delamination, metal ion diffusion and interfacial chemistry, among others.[25-27, 29, 61, 62] M. D. McGehee's group showed that the back electrode replacement could induce a recovery of almost the entire loss of V_{OC} and *FF* in P3HT:PC$_{61}$BM OPVs. A negligible decrease in J_{SC} was still observed, but their samples were annealed throughout the investigation so it is expected that a significant decrease in J_{SC} caused by the absorption and/or diffusion of H_2O would not occur.[63] In our work, the reduction in J_{SC} is larger for the OPV not containing PFI, and a slightly faster decay in J_{SC} is observed for the OPVs with PFI in the twenty three hours of operation after the first half an hour. This suggests that the PFI inhibits the back electrode degradation but neither indefinitely nor completely.

3.3.4. Environmental Monitoring

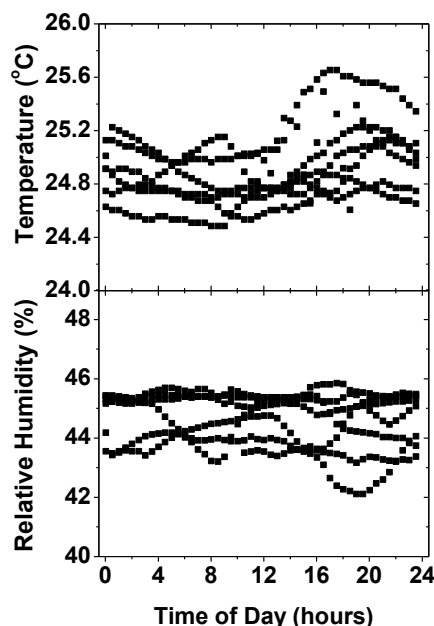Temperature and humidity measurements were carried out whilst performing the degradation study.

Figure S10. Temperature in degrees Celsius **(a)** and Relative humidity in percentage **(b)** recorded under the solar simulator at 30 min time intervals for the course of the degradation study.

These are shown in Figures S10a and S10b, respectively. The measurements were recorded every half an hour for a period of seven days. The environmental conditions are plotted against the time of day at which they were recorded. The mean and standard deviation are 24.94 ± 0.25 $^{\circ}$C and 44.62 ± 0.87 % for the temperature and relative humidity, respectively. Therefore, OPV stability was measured, in accordance with the ISOS-L-1 protocol, with a solar simulator under continuous AM1.5G illumination and ambient conditions as described in Section S1.2.[64]

3.3.5. Normalised Device Characterisations

Figures S11, S12 and S13 show the normalised PCE, V_{OC} and FF, respectively. These are presented for the sake of completeness even though they do not change the conclusions which have previously been drawn in the above sections. The first recorded measurement is used for performing the normalisation, with the exception of FF for the 1:6:1 device, for which the last recorded measurement was used due to the S-kink. The normalised J_{SC} measurements are shown in Figure 8a. In this figure, the initial exponential decay, observed in the first half an hour of operation, has been repressed with the use of PFI. After half an hour of operation the short-circuit current densities, with and without additive, decay at a slower rate. The decays appear to have an initial exponential component, and they become nearly linear after six hours of operation. When no additive is present in the HEL, the PCE decreases by more than 25 % within the first half an hour of operation, as shown in Figure S11. The sharp fall in J_{SC} is largely responsible for the decrease in PCE, as the J_{SC} decreases by ~ 24 % for the same time period. There is a small but noticeable drop in PCE for the devices containing PFI in the first half an hour of operation. This is due to the simultaneous decrease in J_{SC}, V_{OC} and FF. For instance, the use of PFI does not completely stabilise the J_{SC}. Even at the highest concentration of the additive, 1:6:30, the J_{SC} is still reduced by ~ 2.5 % after the first half an hour of

operation. After this initial exponential decay, and over much longer time scale, J_{SC} does decay slightly faster for the OPVs containing PFI even though this kinetic is comparable to the one observed in pristine HEL devices.
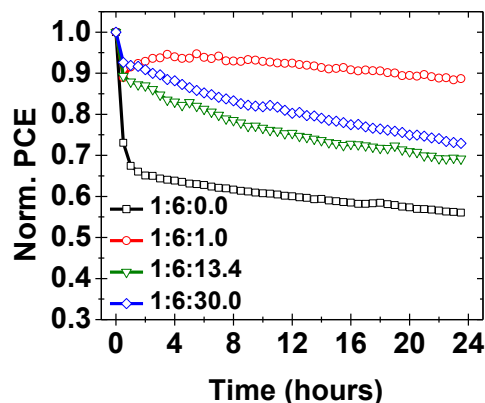

Figure S11. Degradation study: Normalised power conversion efficiency (PCE) for OPV devices with different concentrations of PFI in the PEDOT:PSS based HEL. Data recorded at 30 min time intervals under continuous AM1.5G illumination at 100 mW/cm^2.

Combined with the gradual decrease in V_{OC}, observed in Figure S12, the PCEs for 1:6:13.4 and 1:6:30 degrade somehow faster than the 1:6:0 reference device between the initial exponential decay and the final measurement. The V_{OC} for 1:6:0 has an initial fast exponential decay that extends for an hour, after which the V_{OC} is stable. With PFI, the exponential decay lasts half an hour, and stability is reached after a longer time scale. For instance, the V_{OC} of the 1:6:30 device decays at a slow rate for six hours of operation, when the decay becomes almost linear. The decay in V_{OC} is of smaller amplitude but present a similar trend to that observed for the J_{SC}, as observed when comparing Figure 8a and S12.
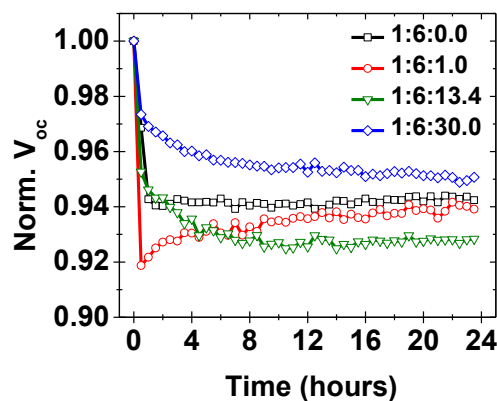

Figure S12. Degradation study: Normalised open-circuit voltage (V_{OC}) for the OPV devices with different concentrations of PFI in the PEDOT:PSS based HEL. Data recorded at 30 min time intervals under continuous AM1.5G illumination at 100 mW/cm^2.

In the unlikely scenario that metal ion diffusion were responsible for the fast exponential decay observed in J_{SC}, a similar prominent decay would be apparent in the V_{OC} and FF.[40] Whilst, there is a fast exponential decay observed in both of these performance parameters, the loss is negligible when compared to that observed in the J_{SC}. The use of PFI does not significantly alter the decay in the V_{OC} and FF, and therefore rules out the possibility that PFI improves device stability by preventing the diffusion of metal ions. The increase in PCE after

half an hour of operation for 1:6:1 is due to an increase in V_{OC} and *FF* as shown in Figures S12 and S13, respectively. The increase gives the impression that 1:6:1 is more stable, however, we have shown that this is only the result of variation compensations related to the initial S-kink J-V characteristic. As previously mentioned, after an hour of operation the V_{OC} for 1:6:0 does not change any more, as shown in Figure S12. However, for 1:6:13.4 and 1:6:30.0, there is a slow decay that lasts approximately six hours. After this period, the V_{OC} of the PFI based devices become stable.
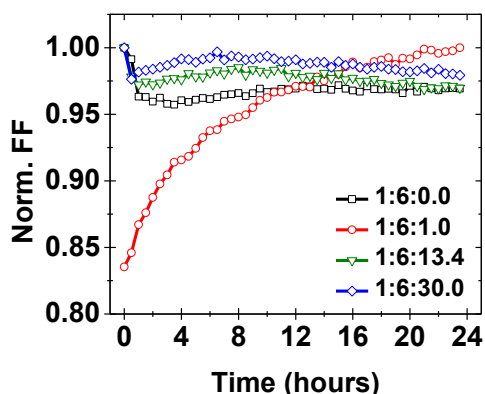

Figure S13. Degradation study: Normalised fill factor (*FF*) for OPV devices with different concentrations of PFI in the PEDOT:PSS based HEL. Data recorded at 30 min time intervals under continuous AM1.5G illumination at 100 mW/cm^2.

The percentage decrease between the initial and final measurement is approximately 5-7 % for all concentrations, and the correlation with the J_{SC} shows that the additive does not prevent indefinitely H$_2$O from eventually altering the properties of the hygroscopic HEL or diffusing to and from the back electrode. Instead, PFI slows down the process indicating an interesting strategy to further develop and optimise the stability of PEDOT:PSS based devices.

The normalised *FF*s, shown in Figure S13, have a similar shape with an initial fast decay followed by a plateau. The former lasts half an hour longer for devices without additive, while the overall variation is of less than 5 %. As previously discussed, at low amount of PFI additive, the time of the initial decay is faster than half an hour, of larger amplitude and the *FF* appears to slowly recover until its value matches with those of the other PFI content devices. This is likely explained by compensating effects associated with the S-kink appearing in the *J-V* characteristics of the low PFI content devices.
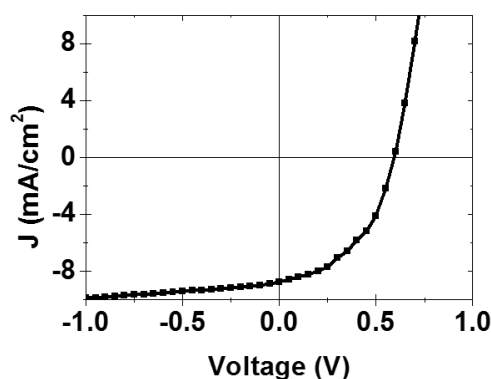

Figure S14. Degradation study: Current-voltage characteristic of the encapsulated P3HT:PC$_{61}$BM device measured at 0 h under AM1.5G illumination at 100 mW/cm^2.

Figure S14 shows the initial current-voltage characteristic of the 2.32 % efficient encapsulated P3HT:PC$_{61}$BM OPV that was used in the degradation study.

The normalised performance parameters for an encapsulated P3HT:PC$_{61}$BM OPV are shown in Figure S15. To appreciate the difference in performance due to encapsulation at the start of the degradation study, only twelve hours of data is shown. After half an hour of operation, the J_{SC} has increased weakly by ~ 1.1 %. It then slowly decays at a considerably slower rate than that observed for any un-encapsulated OPVs. The result reinforces the argument that exposure to H$_2$O significantly impacts the J_{SC}.[45, 63] Therefore, a slower rate of decay is naturally expected with encapsulated OPVs. Half an hour later, one hour into the degradation measurement, the J_{SC} has fallen by 0.14 %. However, the J_{SC} is still 0.96 % higher than the initial measurement. By means of encapsulation, the degradation has gone from being dominated by the Jsc to being dominated by both the V_{OC} and *FF*.

Half an hour into the study the V_{OC} and *FF* have decreased by 2.55 and 1.65 %, respectively. The *FF* for un-encapsulated OPVs without PFI decreases by 1.03 % for the same time period. Therefore, the *FF* for the encapsulated OPV decays at a faster rate. Notably, a faster rate of decay is observed for those OPVs with PFI of > 2 %, hence excluding the low concentration PFI OPV. A possible explanation is that the poor hole extraction at the anode is in balance with poor electron extraction at the cathode due to degradation of the latter on exposure to H$_2$O. The *FF* for the encapsulated OPV continues to degrade further with operation, but at a very slow pace, whereas the one for the un-encapsulated stays constant or even recovers slightly. The decrease in V_{OC} for the un-encapsulated 1:6:0 and 1:6:30 OPVs after half an hour are 3.23 and 2.59 %, respectively. The latter is similar to that acquired for the encapsulated OPV. One hour into the study, the V_{OC} decrease of the encapsulated OPV without PFI and the un-encapsulated with 1:6:30 PFI are comparable and of 3.8 and 3.1 %, respectively. The decrease in V_{OC} is higher, 5.7 %, for un-encapsulated OPVs without PFI. Photo-induced chemical reactions offer a possible explanation as to the mechanism responsible for the decrease in V_{OC} and *FF* in encapsulated P3HT:PC$_{61}$BM OPVs.[45, 47, 65, 66]
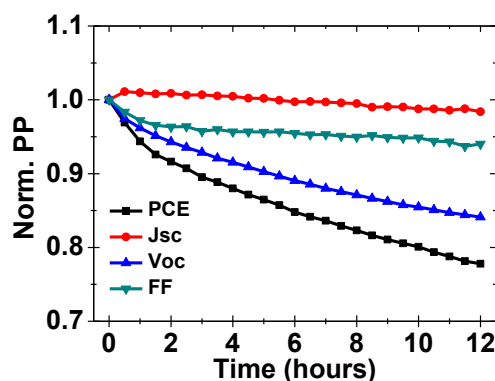

Figure S15. Degradation study: Normalised performance parameters for the encapsulated OPV. Data recorded at 30 min time intervals under continuous AM1.5G illumination at 100 mW/cm^2.

4. Contributions

discussed and carried out the data analysis. HK and DWK were responsible for the AFM and work-function near-field characterisation. Environmental SEM was performed by SS. TA was in charge of the macroscopic Kelvin probe measurements. CTH and PA discussed each set of the data with their contributors and wrote the manuscript under the lead of CTH. Co-authors were able to comment on the sections related to their contributions and provide more general feedback.

5. References

1. D. A. Bonnell, Scanning probe microscopy and spectroscopy : theory, techniques, and applications, Wiley-VCH, New York, 2001.
2. A. Sohn, H. Kim, D.-W. Kim, C. Ko, S. Ramanathan, J. Park, G. Seo, B.-J. Kim, J.-H. Shin and H.-T. Kim, Applied Physics Letters, 2012, **101**, 191605.
3. H. Kim, S. Hong and D.-W. Kim, Applied Physics Letters, 2012, **100**, 022901.
4. C. T. Howells, K. Marbou, H. Kim, K. J. Lee, B. Heinrich, S. J. Kim, A. Nakao, T. Aoyama, S. Furukawa, J.-H. Kim, E. Kim, F. Mathevet, S. Mery, I. D. W. Samuel, A. Al Ghaferi, M. S. Dahlem, M. Uchiyama, S. Y. Kim, J. W. Wu, J.-C. Ribierre, C. Adachi, D.-W. Kim and P. André, Journal of Materials Chemistry A, 2016, **4**, 4252-4263.
5. Y. J. Yu, Y. Zhao, S. Ryu, L. E. Brus, K. S. Kim and P. Kim, Nano Letters, 2009, **9**, 3430-3434.
6. A. F. Stalder, G. Kulik, D. Sage, L. Barbieri and P. Hoffmann, Colloids and Surfaces A: Physicochemical and Engineering Aspects, 2006, **286**, 92-103.
7. N. B. Vargaftik, B. N. Volkov and L. D. Voljak, J. Phys. Chem. Ref. Data, 1983, **12**, 817-820.
8. W. Shockley, The Bell System Technical Journal, 1949, **28**, 435-489.
9. C. J. Brabec, S. E. Shaheen, C. Winder, N. S. Sariciftci and P. Denk, Applied Physics Letters, 2002, **80**, 1288-1290.
10. P. Schilinsky, C. Waldauf, J. Hauch and C. J. Brabec, Journal of Applied Physics, 2004, **95**, 2816-2819.
11. J. Rostalski and D. Meissner, Solar Energy Materials and Solar Cells, 2000, **63**, 37-47.
12. B. Qi and J. Wang, Physical chemistry chemical physics : PCCP, 2013, **15**, 8972-8982.
13. G. J. Hedley, A. J. Ward, A. Alekseev, C. T. Howells, E. R. Martins, L. A. Serrano, G. Cooke, A. Ruseckas and I. D. Samuel, Nat. Commun., 2013, **4**, 2867-2876.
14. W. J. Potscavage, S. Yoo and B. Kippelen, Applied Physics Letters, 2008, **93**, 193308.
15. J. C. Nolasco, A. Sánchez-Díaz, R. Cabré, J. Ferré-Borrull, L. F. Marsal, E. Palomares and J. Pallarès, Applied Physics Letters, 2010, **97**, 013305.
16. V. D. Mihailetchi, L. J. A. Koster and P. W. M. Blom, Applied Physics Letters, 2004, **85**, 970-972.
17. J. C. BERNÈDE, Journal of the Chilean Chemical Society, 2008, **53**, 1549-1564.
18. Y. Li, W. Huang, H. Huang, C. Hewitt, Y. Chen, G. Fang and D. L. Carroll, Sol. Energy, 2013, **90**, 51-57.
19. L. Zuo, J. Yao, H. Li and H. Chen, Solar Energy Materials and Solar Cells, 2014, **122**, 88-93.
20. A. Wagenpfahl, D. Rauh, M. Binder, C. Deibel and V. Dyakonov, Physical Review B, 2010, **82**, 115306.
21. B. Ecker, H.-J. Egelhaaf, R. Steim, J. Parisi and E. von Hauff, The Journal of Physical Chemistry C, 2012, **116**, 16333-16337.
22. A. Kumar, S. Sista and Y. Yang, Journal of Applied Physics, 2009, **105**, 094512.
23. W. Tress, A. Petrich, M. Hummert, M. Hein, K. Leo and M. Riede, Applied Physics Letters, 2011, **98**, 063301.
24. J. Wagner, M. Gruber, A. Wilke, Y. Tanaka, K. Topczak, A. Steindamm, U. Hörmann, A. Opitz, Y. Nakayama, H. Ishii, J. Pflaum, N. Koch and W. Brütting, Journal of Applied Physics, 2012, **111**, 054509.
25. Y. Sun, C. J. Takacs, S. R. Cowan, J. H. Seo, X. Gong, A. Roy and A. J. Heeger, Advanced Materials, 2011, **23**, 2226-2230.
26. L. M. Do, E. M. Han, Y. Niidome, M. Fujihira, T. Kanno, S. Yoshida, A. Maeda and A. J. Ikushima, Journal of Applied Physics, 1994, **76**, 5118-5121.
27. M. Schaer, F. Nüesch, D. Berner, W. Leo and L. Zuppiroli, Advanced Functional Materials, 2001, **11**, 116-121.
28. S. Gardonio, L. Gregoratti, P. Melpignano, L. Aballe, V. Biondo, R. Zamboni, M. Murgia, S. Caria and M. Kiskinova, Org. Electron., 2007, **8**, 37-43.
29. M. T. Lloyd, C. H. Peters, A. Garcia, I. V. Kauvar, J. J. Berry, M. O. Reese, M. D. McGehee, D. S. Ginley and D. C. Olson, Solar Energy Materials and Solar Cells, 2011, **95**, 1382-1388.
30. P. Robaeys, F. Bonaccorso, E. Bourgeois, apos, J. Haen, W. Dierckx, W. Dexters, D. Spoltore, J. Drijkoningen, J. Liesenborgs, A. Lombardo, A. C. Ferrari, F. Van Reeth, K. Haenen, J. V. Manca and M. Nesladek, Applied Physics Letters, 2014, **105**, 083306.
31. T. Nagamori and K. Marumoto, Adv Mater, 2013, **25**, 2362-2367.
32. K. Marumoto and T. Nagamori, Mol Cryst Liq Cryst, 2014, **597**, 29-32.
33. C. T. Howells, Thesis, PhD Doctor of Philosophy, 2015.
34. C. M. Hangarter, S. C. Hernandez, X. He, N. Chartuprayoon, Y. H. Choa and N. V. Myung, Analyst, 2011, **136**, 2350-2358.
35. L. Sun, J. Wang, H.-J. Butt and E. Bonaccurso, Small, 2011, **7**, 950-956.
36. N. Koch, A. Vollmer and A. Elschner, Applied Physics Letters, 2007, **90**, 043512.
37. J. Park, Y. Kwon and T.-W. Lee, Macromol. Rapid Commun., 2007, **28**, 1366-1372.
38. T.-W. Lee, O. Kwon, M.-G. Kim, S. H. Park, J. Chung, S. Y. Kim, Y. Chung, J.-Y. Park, E. Han, D. H. Huh, J.-J. Park and L. Pu, Applied Physics Letters, 2005, **87**, 231106.
39. K.-G. Lim, S. Ahn, Y.-H. Kim, Y. Qi and T.-W. Lee, Energy & Environmental Science, 2016, **9**, 932-939.
40. M. Alsari, Y. M. Omar, M. K. Panda, M. Chiesa, P. Naumov and S. Lilliu, Macromol Chem Physic, 2015, **216**, 1155-1160.
41. T.-H. Lai, S.-W. Tsang, J. R. Manders, S. Chen and F. So, Materials Today, 2013, **16**, 424-432.
42. M. Wang, F. Xie, J. Du, Q. Tang, S. Zheng, Q. Miao, J. Chen, N. Zhao and J. B. Xu, Solar Energy Materials and Solar Cells, 2011, **95**, 3303-3310.
43. S. Olthof, R. Timmreck, M. Riede and K. Leo, Applied Physics Letters, 2012, **100**, 113302.
44. A. Iwan, B. Boharewicz, I. Tazbir, A. Sikora and B. Zboromirska-Wnukiewicz, Int J Photoenergy, 2015, **2015**, 9.
45. K. Kawano, R. Pacios, D. Poplavskyy, J. Nelson, D. D. C. Bradley and J. R. Durrant, Solar Energy Materials and Solar Cells, 2006, **90**, 3520-3530.
46. C. H. Peters, I. T. Sachs-Quintana, J. P. Kastrop, S. Beaupré, M. Leclerc and M. D. McGehee, Adv. Energy Mater., 2011, **1**, 491-494.
47. C. H. Peters, I. T. Sachs-Quintana, W. R. Mateker, T. Heumueller, J. Rivnay, R. Noriega, Z. M. Beiley, E. T. Hoke, A. Salleo and M. D. McGehee, Advanced Materials, 2012, **24**, 663-668.
48. T. Heumueller, W. R. Mateker, I. T. Sachs-Quintana, K. Vandewal, J. A. Bartelt, T. M. Burke, T. Ameri, C. J. Brabec and M. D. McGehee, Energy & Environmental Science, 2014, **7**, 2974.
49. J. Kong, S. Song, M. Yoo, G. Y. Lee, O. Kwon, J. K. Park, H. Back, G. Kim, S. H. Lee, H. Suh and K. Lee, Nat. Commun., 2014, **5**, 5688.
50. A. J. Pearson, P. E. Hopkinson, E. Couderc, K. Domanski, M. Abdi-Jalebi and N. C. Greenham, Org. Electron., 2016, **30**, 225-236.
51. S. Chen, X. Yu, M. Zhang, J. Cao, Y. Li, L. Ding and G. Shi, Journal of Materials Chemistry A, 2015, **3**, 18380-18383.
52. L. Cattin, F. Dahou, Y. Lare, M. Morsli, R. Tricot, S. Houari, A. Mokrani, K. Jondo, A. Khelil, K. Napo and J. C. Bernède, Journal of Applied Physics, 2009, **105**, 034507.
53. T. Hori, T. Shibata, V. Kittichungchit, H. Moritou, J. Sakai, H. Kubo, A. Fujii and M. Ozaki, Thin Solid Films, 2009, **518**, 522-525.
54. G. Li, C. W. Chu, V. Shrotriya, J. Huang and Y. Yang, Applied Physics Letters, 2006, **88**, 253503.
55. T. Stubhan, N. Li, N. A. Luechinger, S. C. Halim, G. J. Matt and C. J. Brabec, Adv. Energy Mater., 2012, **2**, 1433-1438.
56. Y. J. Noh, S. M. Park, J. S. Yeo, D. Y. Kim, S. S. Kim and S. I. Na, ACS Appl Mater Interfaces, 2015, **7**, 25032-25038.
57. M. Manceau, A. Rivaton, J.-L. Gardette, S. Guillerez and N. Lemaître, Polym. Degrad. Stabil., 2009, **94**, 898-907.
58. S. Chambon, A. Rivaton, J.-L. Gardette and M. Firon, Polym. Degrad. Stabil., 2011, **96**, 1149-1158.
59. X. Yang, J. K. J. van Duren, R. A. J. Janssen, M. A. J. Michels and J. Loos, Macromolecules, 2004, **37**, 2151-2158.

60. J. K. J. van Duren, X. Yang, J. Loos, C. W. T. Bulle-Lieuwma, A. B. Sieval, J. C. Hummelen and R. A. J. Janssen, Advanced Functional Materials, 2004, **14**, 425-434.

61. A. M. Hawkridge and J. E. Pemberton, Journal of the American Chemical Society, 2003, **125**, 624-625.

62. F. C. Krebs and K. Norrman, Progress in Photovoltaics: Research and Applications, 2007, **15**, 697-712.

63. I. T. Sachs-Quintana, T. Heumüller, W. R. Mateker, D. E. Orozco, R. Cheacharoen, S. Sweetnam, C. J. Brabec and M. D. McGehee, Advanced Functional Materials, 2014, **24**, 3978-3985.

64. M. O. Reese, S. A. Gevorgyan, M. Jørgensen, E. Bundgaard, S. R. Kurtz, D. S. Ginley, D. C. Olson, M. T. Lloyd, P. Morvillo, E. A. Katz, A. Elschner, O. Haillant, T. R. Currier, V. Shrotriya, M. Hermenau, M. Riede, K. R. Kirov, G. Trimmel, T. Rath, O. Inganäs, F. Zhang, M. Andersson, K. Tvingstedt, M. Lira-Cantu, D. Laird, C. McGuiness, S. Gowrisanker, M. Pannone, M. Xiao, J. Hauch, R. Steim, D. M. DeLongchamp, R. Rösch, H. Hoppe, N. Espinosa, A. Urbina, G. Yaman-Uzunoglu, J.-B. Bonekamp, A. J. J. M. van Breemen, C. Girotto, E. Voroshazi and F. C. Krebs, Solar Energy Materials and Solar Cells, 2011, **95**, 1253-1267.

65. M. Yan, L. J. Rothberg, F. Papadimitrakopoulos, M. E. Galvin and T. M. Miller, Phys Rev Lett, 1994, **73**, 744-747.

66. R. Pacios, A. J. Chatten, K. Kawano, J. R. Durrant, D. D. C. Bradley and J. Nelson, Advanced Functional Materials, 2006, **16**, 2117-2126.